Graphene-supported palladium phosphide PdP_2 nanocrystals for ethanol electrooxidation

Junfeng Liu[a], Zhishan Luo[a], Junshan Li[a], Xiaoting Yu[a], Jordi Llorca[b], Déspina Nasiou[c], Jordi Arbiol[cd], Michaela Meyns[a]*, Andreu Cabot[ad]*

[a] Catalonia Institute for Energy Research (IREC), Sant Adrià de Besòs, 08930 Barcelona, Spain

[b] Institute of Energy Technologies, Department of Chemical Engineering and Barcelona Research Center in Multiscale Science and Engineering, Universitat Politecnica de Catalunya, Eduard Maristany 10-14, 08019 Barcelona, Spain

[c] Catalan Institute of Nanoscience and Nanotechnology (ICN2), CSIC and BIST, Campus UAB, Bellaterra, 08193 Barcelona, Catalonia, Spain

[d] ICREA, Pg. Lluis Companys 23, 08010 Barcelona, Catalonia, Spain

ABSTRACT

We present a procedure to produce pure-phase colloidal PdP_2 nanocrystals (NCs). The approach involves the formation of defective Pd_5P_2 alloy nanoparticles and their posterior crystallization to PdP_2 with further phosphorous incorporation. PdP_2 NCs were supported on reduced graphene oxide and used as electrocatalyst for ethanol oxidation. The activity of PdP_2 for EOR is 3.3 times higher than that of Pd NCs. PdP_2 NCs supported on reduced graphene oxide show further enhanced performance up to 51.4 mA cm^{-2} and mass activity of 1.60 A mg^{-1}_{Pd}, which is 4.8 and 15 times higher than that of Pd NCs, respectively. Besides, PdP_2 NCs and PdP_2/rGO catalysts showed higher stability for EOR than Pd NCs.

INTRODUCTION

Direct liquid fuel cells (DLFC) are electrochemical devices able to directly convert chemical energy stored within liquid fuels into electricity. Among the possible liquids, ethanol shows several advantages, including a high energy density (8.01 KW h kg^{-1}), above that of methanol (6.09 kW h kg^{-1}) and formic acid (1.74 kW h kg^{-1}) [1,2], low toxicity, a relatively high boiling point for safe storage and transportation, and the ability to be bio-sourced in large quantities from the fermentation of biomass. Owing to their several advantages, direct ethanol fuel cells (DEFCs) have become one of the most appealing alternatives to electrochemical batteries and conventional fossil fuel-based combustion engines to give a couple of examples in different application fields. However, the high price and limited performance of current electrocatalysts is limiting their extensive deployment. This limitation, extensive to most fuel cell technologies is particularly severe in DEFCs since compared with the oxidation of methanol or formic acid, the ethanol oxidation reaction

(EOR) is much more complex, involving the release of 12 electrons per molecule and the cleavage of a C-C bond.

Extensive research on electrocatalysts for DEFCs has been carried out on acidic conditions, which allow taking advantage of convenient proton exchange membranes for the device fabrication. However, the slow reaction kinetics and low stability of electrocatalysts in these conditions are very tough barriers to be overcome [3,4]. As an alternative, effort has been moved toward developing electrocatalysts for alkaline-type DEFCs. The enhanced catalytic reaction kinetics in alkaline solution increases the efficiency in the use of precious metals and even enables the use of less expensive catalysts.

Pt and Pt-based alloys have been extensively studied as the most active catalysts for DEFCs. Pd and Pd-based alloys are a significantly more abundant and lower cost alternative to Pt. Pd-based electrocatalysts, such as PdNi [5,6], Pd_2Ru [7] PdCu [8-10], PdAu [11] and Pd_2Sn [4,12], have demonstrated comparable electrocatalytic activities in the electrooxidation of different types of liquid fuels and particularly ethanol. A particularly interesting case is that of Pd-base phosphide which has shown excellent activity toward hydrogen evolution, oxygen reduction, formic acid oxidation and hydrodesulfurization [13,14], and allow improving corrosion resistance while being characterized with high electrical conductivities. However, surprisingly, they have never been investigated as electrocatalysts for the EOR.

Actually, few attempts have been done to produce palladium phosphide NCs at all. Most attempts to produce palladium phosphides has been based on the reaction at relatively high temperatures of premade Pd with a phosphorus precursor such as TOP or white phosphorous [13,15-17]. Following this strategy, quasi amorphous palladium phosphide particles with irregular shapes and broad size distributions are obtained [16,17]. The direct synthesis of monodispersed palladium phosphide NCs has been proven quite challenging. Pure-phase Pd_5P_2 crystallites with a few hundred nanometers were prepared using $Pd(acac)_2$ as metal precursor and TOP as phosphorus precursor [14]. Using the same strategy, Pd_5P_2 nanoparticles encapsulated within mesoporous silica were also prepared [14].

Herein, we report a facile colloidal method to produce colloidal PdP_2 NCs. Compared with the common synthesis method which convert premade metallic Pd into phosphide, our protocol involved the nucleation of Pd_5P_2 and their crystallization and growth into pure-phase PdP_2 NCs with the incorporation of additional P. After ligand exchange, PdP_2 NCs were uniformly deposited on reduced graphene oxide sheets and tested as electrocatalyts for the EOR.

EXPERIMENTAL

Chemicals: Palladium(II) acatylacetonate ($Pd(acac)_2$, Pd 34.7 wt%) and hexamethylphosphoroustriamide (HMPT, 97 %) were purchased from Alfa Aesar. Oleylamine (OAm, approximate C18 content 80-90 %) were purchased from ACROS Organics. Methylamine hydrochloride (MAHC, 98 %), ammonium thiocyanate (NH_4SCN, 99 %) potassium hydroxide (KOH, 85 %), Nafion (5 wt% in a mixture of low aliphatic alcohols and

water), graphite, potassium permanganate ($KMnO_4$, 99 %), sodium nitrate ($NaNO_3$, 99 %), sulfuric acid (H_2SO_4, 95-98 %), hydrochloric acid (HCl, 37 %), hydrogen peroxide (H_2O_2, 30 wt% in H_2O) were obtained from Sigma-Aldrich. Chloroform, ethanol and acetone were of analytical grade and obtained from various sources. MilliQ water was obtained by using a PURELAB flex from ELGA. All chemicals were used as received without further purification.

Synthesis of PdP_2 NCs: In a typical synthesis, 60.9 mg (0.2 mmol) of $Pd(acac)_2$, 67.5 mg (1 mmol) of MAHC, 10 mL of OAm were mixed in a 50 mL Schlenk flask. The reaction system was purged under argon at 120 °C for 1 h. Then 0.1 mL (0.57 mmol) of HMPT was injected into the solution and the temperature was further increased to 300 °C in 20 min. During the heating up, the solution became black at around 250 °C. The flask was maintained at 300 °C for 1 h before the solution was allowed to cool to room temperature. The isolation of the resultant black precipitate was achieved with excess ethanol followed by centrifugation. Purification was achieved by multiple dispersion/precipitation steps using chloroform and ethanol. Finally the powder was suspended in 5 mL of chloroform in a vial.

Caution: *Because this procedure involves the high-temperature decomposition of a phosphorous precursor that can liberate toxic and flammable phosphine gas, the reaction should only be carried out by appropriately trained personnel using rigorously air-free conditions and the Schlenk line should be connected with gas absorption solutions.*

Synthesis of Pd NCs: Pd spherical NCs were prepared by mixing the same amount of $Pd(acac)_2$, MAHC and OAm at the same condition as in the synthesis of PdP_2 NCs but without injection of HMPT. The reaction was kept at 300 °C for 1 h and then washed following the same procedures as in the synthesis of PdP_2.

Synthesis of rGO: Graphene oxide was produced by a modified Hummers method as originally presented by Kovtyukhova [35]. Briefly, in a 500 mL flask, 2 g of graphite, 1.5 g of $NaNO_3$ and 96 mL of concentrated H_2SO_4 were vigorously stirred in ice-water bath. Then, 9 g of $KMnO_4$ was slowly added to the flask over 30 min. Stirring was continued for 1.5 h in the ice-water bath and then followed by another 2 h at 35 °C. Afterward, 280 mL of H_2O was added into the mixture. During the process, the solution was heated to 98 °C and kept at this temperature for 2 h. 5 mL of 30 wt% H_2O_2 was added to the solution after the temperature was decreased to 60 °C. To remove ionic impurities, the obtained solution was washed through vacuum filtering by 3 wt% HCl aqueous for 3 times, followed by H_2O for another 3 times. The resulted product was dried under vacuum at 60 °C and then calcined in a tube furnace at 500 °C for 2 h in flowing argon. As a result, the reduced graphene oxide (rGO) was obtained.

Ligand exchange: The ligand exchange procedure used here was similar to that previously reported by Fafarman et al. [18]. In a typical procedure, 0.5 mL of 130 mM NH_4SCN in acetone was added to 1 mL of a dispersion of as-synthesized PdP_2 NCs in chloroform (~10 mg in 1 mL). The resulted solution was agitated for 1 min, and then a complete flocculation was observed within seconds. The slurry was centrifuged at 3000 rpm for 1 min and the supernatant discarded. Another 1 mL volume of acetone was added to the precipitate, sonicate for 1 min and followed by centrifuge at 3000 rpm for 1 min. The washing steps were

repeated for another time and the obtained precipitate was dried at room temperature.

Catalyst preparation: The catalyst ink for electrochemical measurements was prepared by mixing 5 mg of PdP_2 NCs and 5 mg of rGO in 5 mL of deionized water. The mixture was sonicated for 1 h to form a homogeneous catalyst ink. For comparison, catalysts of Pd and PdP_2 were also prepared through dissolving 10 mg of as-synthesized Pd or PdP_2 NCs in 5 mL of deionized water by sonication for 1 h.

The working electrode was prepared using a glassy carbon electrode (GCE, 5 mm in diameter) which was previously polished using diamond paper and 0.05 µm alumina slurry sequentially, followed by ultrasonication in ethanol first and water later, for 1 min each. The cleaned GCE was dried under argon flow at room temperature. The electrode was modified by drop casting 10 µL of the catalyst ink and posterior drying at room temperature. To immobilize the catalysts on the electrode, 10 µL of a 0.5 wt% Nafion solution was droped on the surface of the electrode.

Electrochemical measurements: Electrochemical measurements were conducted at room temperature on a BioLogic electrochemical workstation using a standard three-electrode cell with the modified GCE as working electrode, a Pt mesh as counter electrode and Hg/HgO (1 M KOH) as reference electrode. All the CV measurements were conducted at room temperature. The electrolyte solutions were purged with argon for 30 min before use. The background was obtained by CV measurement in 0.5 M KOH solution from -1.0 to 0.3 V vs. Hg/HgO at 50 mV s^{-1}. Afterward, for EOR measurement, the working electrodes were tested in 0.5 M KOH with 0.5 M ethanol solution under the same conditions. The chronoamperometry measurements were conducted at -0.1 V vs. Hg/HgO for 4000s in the electrolyte of 0.5 M KOH and 0.5 M ethanol in order to evaluate the stability of the catalysts.

Characterization: Transmission electron microscopy (TEM) characterization was carried out using a ZEISS LIBRA 120, operating at 120 kV and a JEOL 1011 operating at 100 kV. Carbon-coated TEM grids from Ted-Pella were used as substrates. High-resolution TEM (HRTEM) studies were conducted using a field emission gun FEITM Tecnai F20 microscope at 200 kV with a point-to-point resolution of 0.19 nm. Annular dark-field (HAADF) STEM was combined with electron energy loss spectroscopy (EELS) in the Tecnai F20, by using a GATAN QUANTUM filter. Scanning electron microscopy (SEM) analyses were done in a ZEISS Auriga microscope with an energy dispersive X-ray spectroscopy (EDS) detector operating at 20 kV. Powder X-ray diffraction (XRD) patterns were collected directly from the as-synthesized nanoparticles dropped on Si (501) substrate on a Bruker-AXS D8 Advanced X-ray diffractometer with Ni-filtered (2 µm thickness) Cu K radiation (λ = 1.5406 Å) operating at 40 kV and 40 mA. A LynxEye linear position-sensitive detector was used in reflection geometry. X-ray photoelectron spectroscopy (XPS) was done on a SPECS system equipped with an Al anode XR50 source operating at 150 mWand a Phoibos 150 MCD-9 detector. The pressure in the analysis chamber was below 10^{-7} Pa. The area analyzed was about 2 mm × 2 mm. The pass energy of the hemispherical analyzer was set at 25 eV and the energy step was set at 0.1 eV. Data processing was performed with the CasaXPS program (Casa Software Ltd., UK). Binding energy values were centered using the C 1s peak at 284.8 eV. Fourier transform infrared spectroscopy (FTIR) was performed

on an Alpha Bruker FTIR spectroscopy with a platinum attenuated total reflectance (ATR) single reflection module. FTIR spectra data were recorded from 400 cm^{-1} to 4000 cm^{-1}.

RESULTS AND DISCUSSION

1.1. NC synthesis

PdP_2 NCs were produced within OAm from the reaction of $Pd(acac)_2$ as Pd precursor with HMPT as P source in the presence of MAHC (see details in the experimental section). All elements were introduced in the reaction flask at a low temperature and the reaction mixture was heated up to 300 °C. During the heating up process, the solution became black at around 250 °C, pointing at a product formation at this temperature. Spherical nanoparticles with a highly defective/disordered Pd_5P_2 phase and an average size of 7 nm were recovered from aliquots extracted after 1 min reaction at 300 °C (**Figure S1**). As the reaction time increased, additional P was progressively incorporated into the Pd_5P_2 nanoparticles, which crystallized into elongated PdP_2 NCs (**Figure S1**).

Figure 1a shows a TEM micrograph of the NCs obtained after 1h reaction at 300 °C. NCs showed elongated, tear drop-like geometry and had an average size of its longer axis of 12 ± 2 nm. XRD patterns showed the NCs to have a PdP_2 monoclinic phase, with I2/c space group (**Figure 1b**). No additional XRD peaks corresponding to secondary crystal phases were detected. HRTEM analysis confirmed the monoclinic phase of the NCs and allowed determining the lattice parameters: a = 6.207 Å, b = 5.857 Å and c = 5.874 Å (**Figure 2a**). Annular dark field scanning TEM (ADF-STEM) and STEM-EELS elemental composition maps revealed all NCs to contain Pd and P and to have both elements uniformly distributed throughout each NC (**Figure 2b**). SEM-EDS analysis showed the NCs to have an atomic ratio of P/Pd = 2.0 ± 0.1 (**Figure S2**).

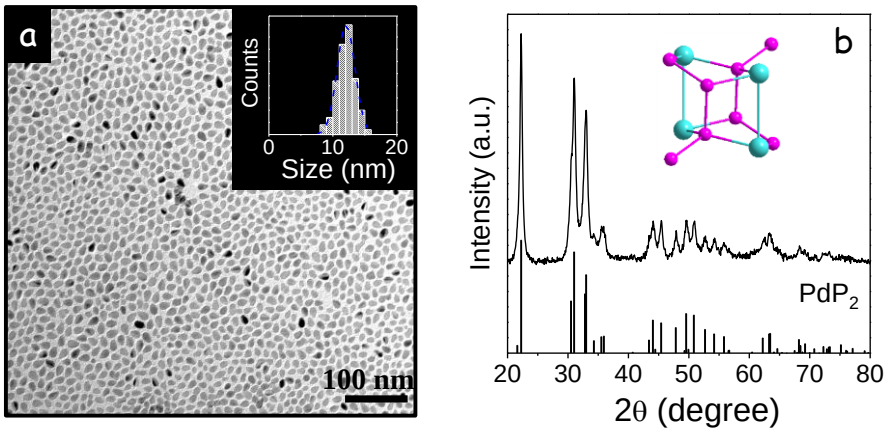

Figure 1. a) Representative TEM micrograph of PdP_2 NCs. Inset shows their size (long axis) distribution histogram. b) XRD pattern of PdP_2 NCs including the JCPDS 77-1421 reference. Inset shows a unit cell of the PdP_2 monoclinic phase (Pd in blue and P in pink).

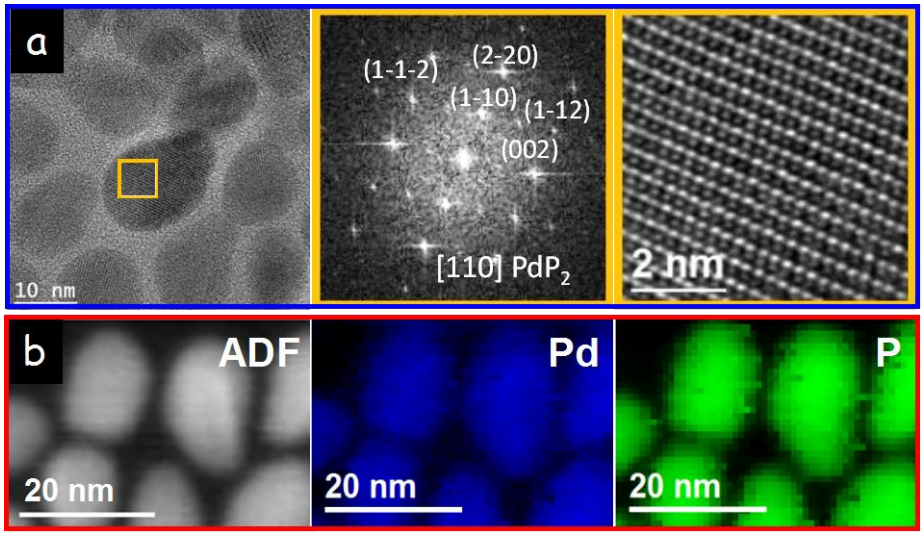

Figure 2. a) HRTEM image of several PdP_2 NCs and power spectrum fitting with the PdP_2 phase of one of them. b) ADF-STEM image of several PdP_2 NCs and EELS compositional maps for Pd (blue) and P (green).

To determine the role of MAHC in the synthesis, the reaction was performed in the absence of this compound. In these conditions, before adding the P precursor, the solution changed to black at 120 °C, during the heating up process. XRD analysis of the recovered solid showed that it consisted of Pd (**Figure S3**). Therefore, in the absence of MAHC, the Pd precursor is reduced by OAm at low temperature, resulting in the formation of Pd NCs. Once HMPT was injected in the solution containing the reduced Pd precursor, Pd NCs reacted with P to produce very small Pd-P nanoparticles, which after reaction at 300 °C for 1 h resulted in 5 nm Pd_5P_2 and PdP_2 NCs mixture (**Figure S4**).

In the presence of 0.2 mmol of MAHC, colloidal NPs were obtained at higher temperature, about 250 °C, indicating that the present of MAHC prevented the reduction by OAm. After reacting at 300 °C for 1 h, teardrop shaped PdP_2 NCs with some spherical Pd_5P_2 NPs were obtained. With the increasing amount of MAHC, the shape of as-synthesized nanoparticles turned uniform and less spherical Pd-P amorphous nanoparticles were observed in the products (**Figure S5**). This last point was followed by the decrease of the XRD band at about $2\theta = 40°$ assigned to a disordered/defective Pd_5P_2 phase (**Figure S6**), which was observed to decrease with the amount of MAHC introduced. This band completely disappeared when 1 or 2 mmol MAHC were present in the reaction system. At this point, pure phase PdP_2 NCs were obtained.

To elucidate the role of chlorine and the amine group of MAHC, the synthesis was carried out in the presence of NH_4Cl instead of MAHC. In these conditions, a similar reaction temperature, as observed from the color change of the solution, and a similar product was obtained (**Figure S7**). This experimental results points towards Cl^- ions having a role on the stabilization of the Pd precursor in solution, preventing its reduction with OAm and yielding pure phase PdP_2 when reacting with the P source.

To determine the role of P precursor, HMPT was replaced by TOP. Using TOP, no NPs were obtained at 300 °C, which we associated to the much lower reactivity of TOP when compared with HMPT. When reacting at 350 °C for 1 h, irregular and large-size NCs was obtained (**Figure S8**). XRD and EDS showed a mixture of Pd_5P_2 and PdP_2 phase (**Figure S9**). In this case, the product NPs were irregular in shape, polydisperse in size and phase.

Figure 3 shows the Pd 3d and the P 2p XPS spectra of the PdP_2 NCs. Two doublets were fitted to the Pd 3d states. The main Pd component, accounting for ca. 64 % of the total Pd detected, was found at a Pd $3d_{5/2}$ binding energy 335.9 eV. This binding energy was slightly above that of Pd(0) in pure Pd (335.1-335.5 eV)[18,19], which is consistent with the chemical environment of Pd within a Pd phosphide. A more oxidized component, accounting for ca. 36% of the Pd detected, was found at a Pd $3d_{5/2}$ binding energy of 337.7 eV. This component was assigned to Pd(II) species at the surface of the air-exposed NCs that had undergone oxidation [20].

Two P chemical states were also identified from XPS analysis of the P 2p electronic states. A main P $2p_{3/2}$ peak at 130.3 eV matched well with P in a metal phosphide environment. This component accounted for ca. 64 % of the detected P. The second component, accounting for ca. 36 % of the P detected, was found at a higher binding energy, P $2p_{3/2}$ peak at 134.1 eV, and it was assigned to a phosphate environment. We believe this phosphate to result from the partial oxidation of the PdP_2 surface due to air exposure [21-23].

The atomic ratio of Pd and P at the NC surface detected by XPS was approximately 1, which pointed toward a Pd enriched surface compared to the PdP_2 core.

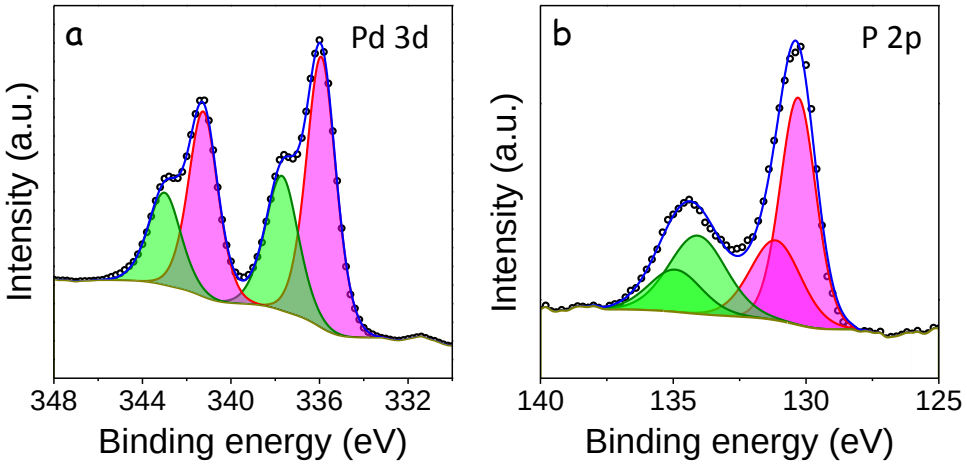

Figure 3. XPS spectra of PdP_2 NCs in the Pd 3p (a) and P 2p (b) regions.

1.2. NC surface treatment and catalyst preparation

FTIR spectra of as-produced PdP_2 NCs displayed peaks at 2920 and 2852 cm^{-1} attributed to the C-H stretching vibration of the alkyl group of OAm (**Figure 4**). Additionally, peaks attributed to the bending vibration of C-H in alkyl and alkenyl part of OAm, at 1457 and 968 cm^{-1}, and to the bending vibrations of

N-H and C-N, at 1551 and 1059 cm^{-1}, were also identified. These features were slightly shifted compared with pure OAm, consistently with its binding to the NC surface. While the presence of OAm at the NC surface render the NCs colloidally stable in non-polar solvents and limited their growth, OAm might also block catalytic sites and hinder charge transfer, and thus it had to be removed prior to NC catalytic application.

OAm was displaced from the NC surface using a short inorganic ligand, ammonium thiocyanate, following the procedure reported by Fafarman et al. (see experimental section for details) [18]. FTIR spectra of the NCs after ligand displacement with ammonium thiocyanate showed the presence of peaks at 2045 and 1596 cm^{-1}, assigned to the C≡N antisymmetric and asymmetric vibration, and a broad peak at ca. 1400 cm^{-1} corresponding to the N-H stretching vibration of the amino group of NH_4SCN.

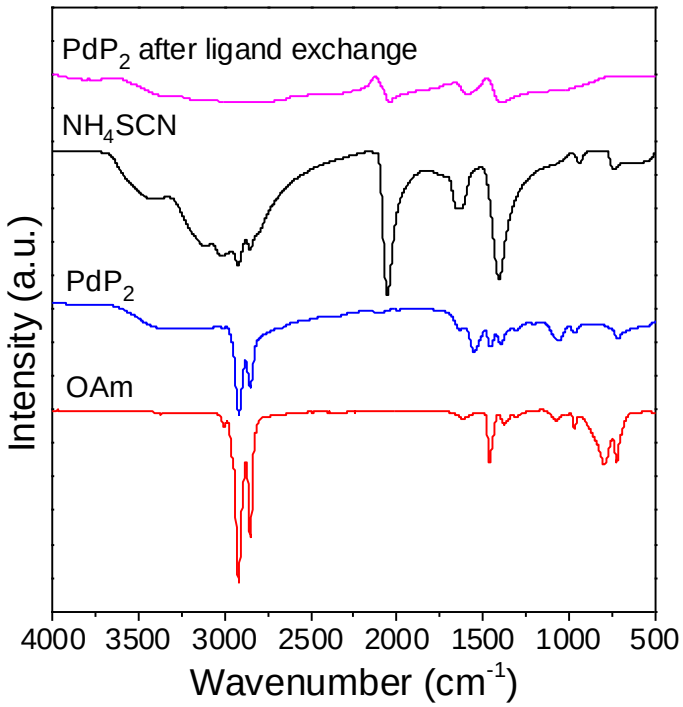

Figure 4. FTIR of OAm, NH_4SCN, as-synthesized PdP_2 NCs and PdP_2 after ligand exchange by NH_4SCN.

Electrocatalysts were prepared by supporting the colloidal PdP_2 NCs onto rGO. Graphene is considered an ideal electrocatalyst support owing to its excellent electric conductivity, large surface area, superior mechanical flexibility and chemical stability [24]. The use of graphene as the support material not only improves the conductivity of the hybrid catalysts, but also increases the dispersion of the active components, which is helpful to prevent their aggregation during the catalytic reaction. GO sheets were prepared here by a modified Hummers method as presented by Kovtyukhova [25], and then reduced to rGO at high temperature (**Figure S10**). rGO exhibited a rippled and crumpled morphology and paper-like structure with single or few layers (**Figure 5**), offering a large surface area to support the PdP_2 NCs. PdP_2 NCs were supported in the desired concentration by mixing proper amounts of rGO and PdP_2 NCs in water. The nanocomposite was drop-casted onto GCE and then dried at room temperature. On top of it, Nafion

was deposited to immobilize the catalysts on the electrode (see details in the experimental section). As shown in **figure 5**, after solvent removal, PdP_2 NCs were homogeneously distributed on the rGO sheet.

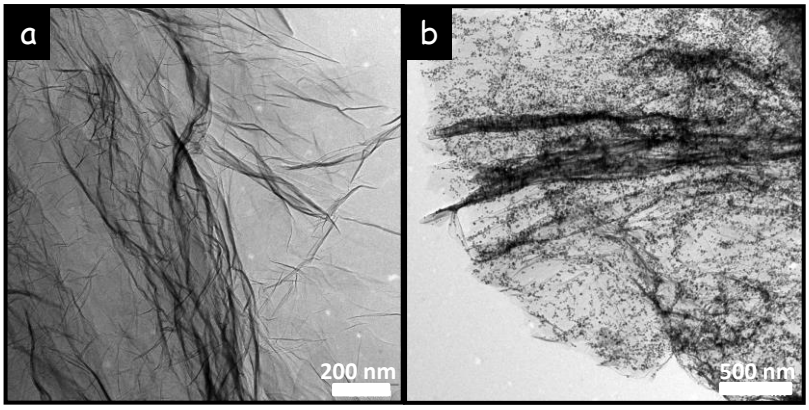

Figure 5. TEM images of as-prepared rGO (a) and PdP_2/rGO catalyst.

1.3. Cyclic voltammetry in base solution

The cyclic voltammetry (CV) of as-prepared PdP_2/rGO electrocatalysts and of 12 ± 3 nm Pd (**Figure S11**) and unsupported PdP_2 as reference were initially investigated in a 0.5 M KOH aqueous solution (**figure 6a**). The same total amount of catalyst was used to produce each of the tested electrodes, which translated into significantly lower amounts of Pd in the PdP_2 and especially on the PdP_2/rGO catalysts.

All catalysts showed similar coulombic features, but with small differences in relevant regions of the voltammograms. The peaks in the region between -0.6 V and -0.8 V vs. Hg/HgO are attributed to the adsorption (cathodic scan) and desorption (anodic scan) of hydrogen. In the anodic scan, the PdP_2 catalyst showed a positive shift of peak potentials compared to Pd, while in the cathodic scan, the PdP_2 showed a slight negative shift of the cathodic peak potential. The distinct anodic and cathodic behaviors on PdP_2 and Pd catalysts were related to their different electronic structure involving partial electron donation from Pd to P sites, as also observed from XPS.

The peaks in the anodic scan region from -0.4 to -0.2 V vs. Hg/HgO were attributed to the formation of palladium oxide on the NCs surface. Subsequently, oxide reduction peaks showed up at about -0.2 V vs. Hg/HgO during the negative scans. The electrochemically active surface area (ECSA) of the catalysts was estimated from the coulombic charge for the reduction of palladium oxide, i.e. from the area over the voltammetry curve in the PdO reduction peak region [12]:

$$\mathrm{ECSA} = \frac{\mathrm{Q}\,(\mu C \cdot cm^{-2})}{Q_{PdO}(\mu C \cdot cm_{Pd}^{-2}) \times Pd_{loading}(mg \cdot cm^{-2}) \times 10} \qquad (1)$$

where Q_{PdO} = 405 μC cm^{-2} is the charge value given for the reduction of a PdO monolayer, the coulombic charge Q is calculated by integrating the reduction peak area of PdO to Pd, and $Pd_{loading}$ is the Pd mass on the working electrode.

ECSA values obtained for Pd, PdP_2, and PdP_2/rGO catalysts were 49.4 $m^2 g^{-1}$, 97.9 $m^2 g^{-1}$, and 105.1 $m^2 g^{-1}$, respectively. The Pd utilization effectiveness was estimated taking into account that the active surface area for full utilization of 1 g of Pd was 448 m^2 [12,26]. Thus, the Pd utilization efficiencies of PdP_2, PdP_2/rGO and Pd were 21.8 %, 23.4 % and 11.0 %, respectively (**Figure 6e**).

Besides slight differences related to the different geometric of PdP_2 and Pd NCs, the enhanced ECSA and Pd utilization efficiency of PdP_2 over Pd points at a highly Pd rich surface, even beyond XPS-obtained ratios. The oxidation of PdP_2 beyond the surface monolayer could also in part explain the higher ECSA obtained for PdP_2. Besides, the slightly improved Pd utilization efficiency of PdP_2/rGO over unsupported PdP_2 might be attributed to the high surface area of rGO which allows a better dispersion of the PdP_2 NCs.

1.4. Cyclic voltammetry in ethanol solution

The EOR electrocatalytic activities of Pd, PdP_2 and PdP_2/rGO catalysts were investigated in a 0.5 M KOH and 0.5 M ethanol aqueous solution (**figure 6b**). CVs from all catalysts showed the two well defined anodic peaks associated with the ethanol oxidation in alkaline media, one in the forward and the other one in the reverse scan. The oxidation peak in the forward scan is associated with the oxidation of freshly chemisorbed species coming from ethanol adsorption. The oxidation peak in the reverse scan is related to the removal of carbonaceous species not completely oxidized in the forward scan.

The ethanol oxidation process takes place through parallel pathways as shown below [7]:

$$CH_3CH_2OH \rightarrow CH_3CH_2OH_{(ad)} \rightarrow CH_3CHO \rightarrow CH_3COOH \qquad (2)$$

$$CH_3CH_2OH \rightarrow CH_3CH_2OH_{(ad)} \rightarrow CO_{(ad)}, CH_{x(ad)} \rightarrow CO_2 \qquad (3)$$

In equation 2 (C2 pathway), the ethanol is first oxidize to acetaldehyde and further oxidized to acetic acid or acetate in alkaline solution, while the C-C bond is not broken during this pathway. In the equation 3 (C1 pathway), C-C bond is broken and intermediate species such as CO and CH_x fragments are produced, which can be further oxidized to CO_2 or carbonate in alkaline solution.

During the positive scan, to reach a current density of 1 mA cm^{-2}, overpotential of -0.48 V and -0.45 V vs. Hg/HgO are required for PdP_2/rGO and PdP_2, respectively, which is less than for Pd NCs (-0.41 V vs. Hg/HgO), indicating lower activation energy for ethanol oxidation. The forward oxidation current peaked at around -0.12 V vs. Hg/HgO for Pd, -0.09 V for PdP_2 and -0.04 V for PdP_2/rGO (Table 1). Higher potentials resulted in a decrease of current density associated with the oxidation of the Pd surface. At the forward peak current, current densities for the EOR in Pd, PdP_2 and PdP_2/rGO were 10.6, 22.1 and 51.4 mA cm^{-2}, respectively. When the values were normalized to reflect the amount of Pd, the mass peak current density of PdP_2 and PdP_2/rGO were 0.344 and 1.60 A mg_{Pd}^{-1}, respectively, which is ca. 3.3 and 15 times higher than that of Pd (0.104 A mg_{Pd}^{-1}) (**Figure 6f**). Overall, PdP_2/rGO showed high specific and mass activities toward the EOR, comparable to the best Pt- and Pd-based catalysts reported to date (**Figure 7**).

The ratio of oxidation current density peak (j_f) and the backward anodic peak current (j_b) were measured to determine the reaction pathway. A higher j_f/j_b indicates a more efficient oxidation of ethanol and less accumulation of carbonaceous species on the catalyst. As calculated from **figure 6b**, the j_f/j_b ratio for Pd, PdP_2 and PdP_2/rGO were 0.82 to 0.99 and 1.22, respectively (**Table 1**). The increased ratio suggested more efficient ethanol oxidation process for PdP_2 and PdP_2/rGO than Pd.

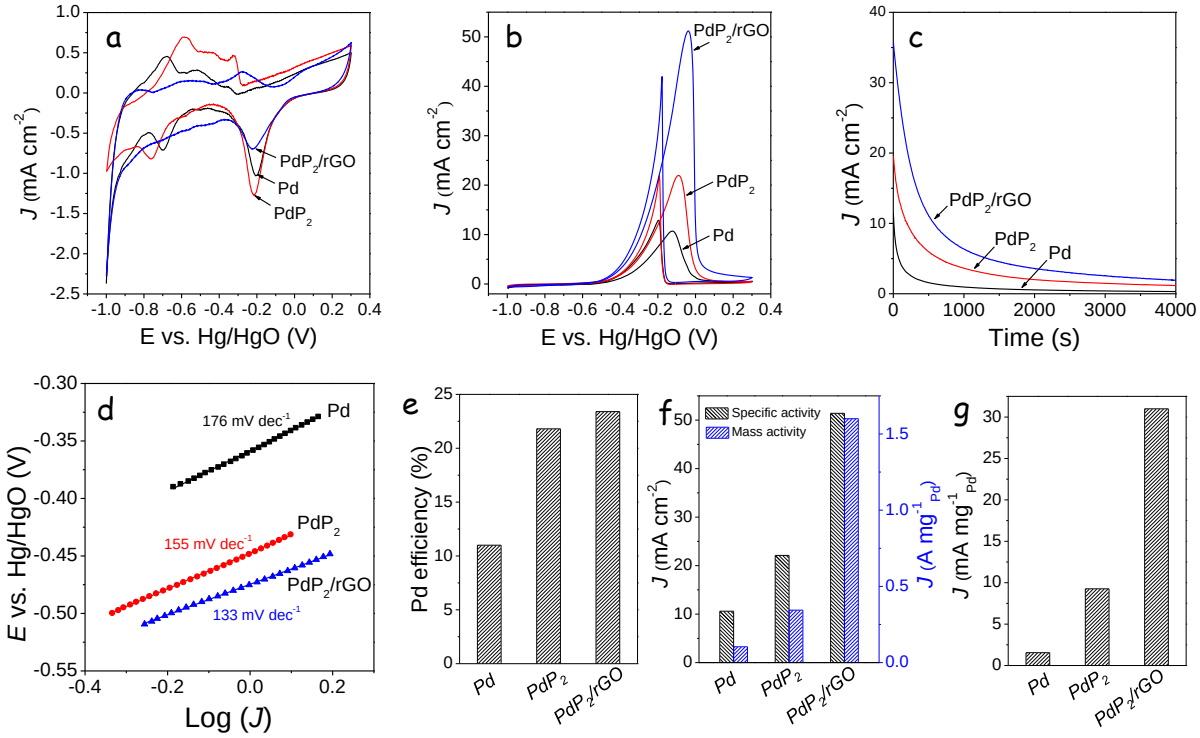

Figure 6. (a) Cyclic voltammetric measurements of Pd, PdP_2 and PdP_2/rGO in a 0.5 M KOH solution and (b) in a 0.5 M KOH + 0.5 M ethanol solution. (c) Chronoamperometric measurements of Pd, PdP_2 and PdP_2/rGO in a 0.5 M KOH + 0.5 M ethanol solution at -0.1 V vs. Hg/HgO. (d) Tafel plot of the Pd, PdP_2 and PdP_2/rGO. (e) Comparison of palladium utilization efficiencies. (f) Comparison of specific activity and mass acivity of the Pd, PdP_2 and PdP_2/rGO and (g) the mass activity after chronoamperometric measurements for 4000 s.

Table 1. Maximum J and V of the maximum J for the forward and reverse scans ratio of Jmax between the forward and reverse oxidation peaks

Catalysts	Forward Scan		Reverse Scan		J_f/J_b
	E_f (V vs. Hg/HgO)	J_f (mA cm^{-2})	E_b (V vs. Hg/HgO)	J_b (mA cm^{-2})	
Pd	-0.12	10.6	-0.194	12.9	0.82
PdP_2	-0.09	22.1	-0.192	22.3	0.99
PdP_2/rGO	-0.04	51.4	-0.178	42.1	1.22

Chronoamperometry (CA) was employed in a solution of 0.5 M KOH + 0.5 M ethanol with a constant applied potential of -0.1 V vs. Hg/HgO to evaluate the stability of catalysts. As displayed in **figure 6c**, initial rapid decreases in current density were observed for all the catalysts, followed by a sluggish decrease until a pseudo-steady state. The sharp initial decrease was ascribed to the absorption and accumulation of strongly adsorbed reaction intermediates on the surface of free active sites. Subsequently, the absorption of ethanol depends on the liberation of the active sites resulted from the oxidation of ethanol or intermediates that formed during the initial state. After 4000 s activity, the current obtained for PdP_2 (1.17 mA cm^{-2}) and PdP_2/rGO (1.96 mA cm^{-2}) was much higher than that of Pd NPs (0.31 mA cm^{-2}). When comparing by mass activities, PdP_2/rGO (31 mA mg^{-1}_{Pd}) and PdP_2 (9.3 mA mg^{-1}_{Pd}) showed about 20 and 6 times higher values than Pd (1.55 mA mg^{-1}_{Pd}) (**Figure 6g**).

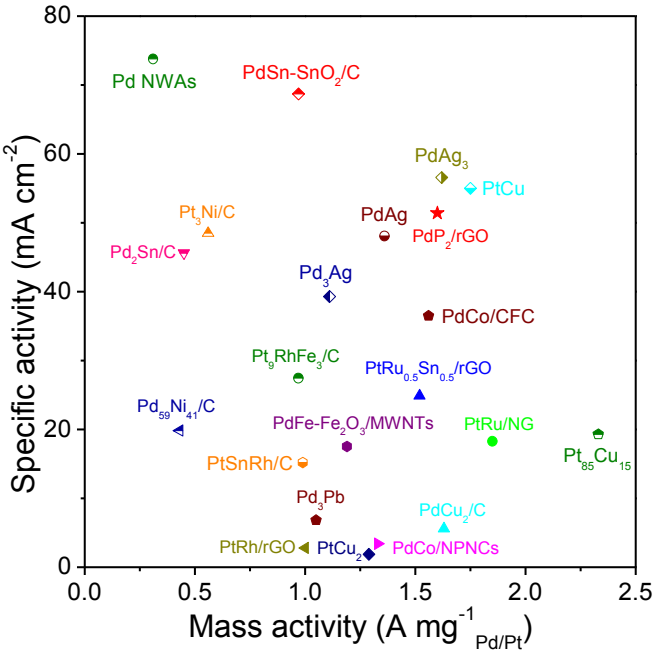

Figure 7. Specific activity and mass activity of PdP_2/rGO in this work compared with reported catalysts Pt_3Ni/C (ref. 27), PtRu/NG (ref. 28), $PtCu_2$ (ref. 29), PtRh/rGO (ref. 30), Pt_9RhFe_3/C (ref. 31), $PtRu_{0.5}Sn_{0.5}$ (ref. 32), Pd_2Sn/C (ref. 4), $Pd_{59}Ni_{41}$/C (ref. 33), Pd_3Pb (ref. 34), PdCo/NPNCs (ref. 35), $PdCu_2$/C (ref. 36), PdFe-Fe_2O_3/MWNTs (ref. 37), $Pt_{85}Cu_{15}$ (ref. 38), Pd NWAs (ref. 39), PtCo/CFC (ref. 40), $PdAg_3$, PdAg and Pd_3Ag (ref. 41), PtCu (ref. 42), PtSnRh/C (ref. 43), PdSn-SnO_2/C (ref. 44). Abbreviations: reduced graphene oxide (rGO), N-doped graphene (NG), N-doped porous carbon nanocapsules (NPNCs), multiwalled carbon nanotubes (MWNTs), nanowire arrays (NWAs) and carbon fiber cloth (CFC).

Figure 6d shows a linear region of the Tafel plots obtained from the CV curves in the region from -0.5 to -0.3 V vs. Hg/HgO. As the potential further increased above -0.2 V, the Tafel plot becomes curved, indicating a change in the factor limiting the reaction rate. As shown in **figure 6d**, Pd NPs showed a Tafel slope of 176 mV dec^{-1}, well above that of PdP_2 and PdP_2/rGO, with Tafel slopes of 155 and 133 mV dec^{-1}, respectively. These values were close to the theoretical value (120 mV dec^{-1}) [45]. The lower Tafel slopes

indicated that the charge-transfer kinetics of the EOR on the PdP_2 and PdP_2/rGO catalysts were faster than that on Pd in the alkaline medium, which can be ascribed to the positive effect of P on the electronic state of Pd, the enhanced electron conductivity and uniform dispersion of PdP_2 NPs on rGO.

2. CONCLUSIONS

In summary, pure-phase, monodisperse PdP_2 NCs with tear drop shape were produced in the presence chlorine ions and using a high activity of P precursor, HMPT. PdP_2 NCs showed high mass activity and long-term stability toward ethanol oxidation in alkaline media. The enhanced properties can be attributing to the effect of P on the electronic state of Pd and the high Pd content at the surface. The activity and stability of catalyst were further improved by supporting PdP_2 NCs onto rGO due to the enhanced conductivity, crumpled structure and uniform dispersion of PdP_2 NCs on rGO. The slower current decay over time combined with the higher measured activity for PdP_2 and PdP_2/rGO indicated a higher tolerance to the carbonaceous species formed.

Appendix A. Supplementary material

Supplementary data associated with this article can be found in the online version at: Additional experimental data

Notes

The authors declare no competing financial interest.

Acknowledgements

D. Nasiou and J. Arbiol acknowledge funding from Generalitat de Catalunya 2017 SGR 327 and the Spanish MINECO project VALPEC (ENE2017-85087-C3). ICN2 acknowledges support from the Severo Ochoa Programme (SEV-2013-0295) and is funded by the CERCA Programme / Generalitat de Catalunya. J. Llorca is a Serra Hunter Fellow and is grateful to ICREA Academia program and grants MINECO/FEDER ENE2015-63969-R and GC 2017 SGR 128. J. Liu, J. Li and X. Yu thank the China Scholarship Council for scholarship support. M. Meyns acknowledges a Juan de la Cierva formación grant by the Spanish MINECO.

References

[1] S.T. Nguyen, H.M. Law, H.T. Nguyen, N. Kristian, S. Wang, S.H. Chan, X. Wang, Enhancement effect of Ag for Pd/C towards the ethanol electro-oxidation in alkaline media, Appl. Catal. B - Environ., 91 (2009) 507-515.

[2] W. Hong, J. Wang, E. Wang, Facile synthesis of highly active PdAu nanowire networks as self-supported electrocatalyst for ethanol electrooxidation, ACS Appl. Mater. Inter., 6 (2014) 9481-9487.

[3] F. Ren, H. Wang, C. Zhai, M. Zhu, R. Yue, Y. Du, P. Yang, J. Xu, W. Lu, Clean method for the synthesis of reduced graphene oxide-supported PtPd alloys with high electrocatalytic activity for ethanol oxidation in alkaline medium, ACS Appl. Mater. Inter., 6 (2014) 3607-3614.

[4] Z. Luo, J. Lu, C. Flox, R. Nafria, A. Genç, J. Arbiol, J. Llorca, M. Ibáñez, J.R. Morante, A. Cabot, Pd2Sn [010] nanorods as a highly active and stable ethanol oxidation catalyst, J. Mater. Chem. A, 4 (2016) 16706-16713.

[5] Z. Chen, J. Zhang, Y. Zhang, Y. Liu, X. Han, C. Zhong, W. Hu, Y. Deng, NiO-induced synthesis of PdNi bimetallic hollow nanocrystals with enhanced electrocatalytic activities toward ethanol and formic acid oxidation, Nano Energy, 42 (2017) 353-362.

[6] B. Cai, D. Wen, W. Liu, A.K. Herrmann, A. Benad, A. Eychmuller, Function-Led Design of Aerogels: Self-Assembly of Alloyed PdNi Hollow Nanospheres for Efficient Electrocatalysis, Angew. Chem. Int. Edit., 54 (2015) 13101-13105.

[7] J. Guo, R. Chen, F.-C. Zhu, S.-G. Sun, H.M. Villullas, New understandings of ethanol oxidation reaction mechanism on Pd/C and Pd2Ru/C catalysts in alkaline direct ethanol fuel cells, Appl. Catal. B - Environ., 224 (2018) 602-611.

[8] K. Jiang, P. Wang, S. Guo, X. Zhang, X. Shen, G. Lu, D. Su, X. Huang. Ordered PdCu-Based Nanoparticles as Bifunctional Oxygen-Reduction and Ethanol-Oxidation Electrocatalysts, Angew. Chem. Int. Ed. 2016, 55, 9030-9035.

[9] X. Zhao, L. Dai, Q. Qin, F. Pei, C. Hu, N. Zheng, Self-Supported 3D PdCu Alloy Nanosheets as a Bifunctional Catalyst for Electrochemical Reforming of Ethanol, Small, 13 (2017) 1602970.

[10] C. Hu, X. Zhai, Y. Zhao, K. Bian, J. Zhang, L. Qu, H. Zhang, H. Luo, Small-sized PdCu nanocapsules on 3D graphene for high-performance ethanol oxidation, Nanoscale, 6 (2014) 2768-2775.

[11] J. Liu, Y. Zheng, Z. Hong, K. Cai, F. Zhao, H. Han. Microbial synthesis of highly dispersed PdAu alloy for enhanced electrocatalysis. Sci. Adv., 2 (2016) e1600858.

[12] C. Wang, Y. Wu, X. Wang, L. Zou, Z. Zou, H. Yang, Low temperature and surfactant-free synthesis of Pd2Sn intermetallic nanoparticles for ethanol electro-oxidation, Electrochim. Acta, 220 (2016) 628-634.

[13] A.R.J. Kucernak, K.F. Fahy, V.N.N. Sundaram, Facile synthesis of palladium phosphide electrocatalysts and their activity for the hydrogen oxidation, hydrogen evolutions, oxygen reduction and formic acid oxidation reactions, Catal. Today, 262 (2016) 48-56.

[14] G.H. Layan Savithra, R.H. Bowker, B.A. Carrillo, M.E. Bussell, S.L. Brock, Mesoporous matrix encapsulation for the synthesis of monodisperse Pd5P2 nanoparticle hydrodesulfurization catalysts, ACS Appl. Mater. Inter., 5 (2013) 5403-5407.

[15] A. E. Henkes, Y. Vasquez, R. R. Schaak. Converting Metals into Phosphides: A General Strategy for the Synthesis of Metal Phosphide Nanocrystals. J. Am. Chem. Soc. 2007, 129, 1896-1897.

[16] S. Carenco, Y. Hu, I. Florea, O. Ersen, C. Boissiere, C. Sanchez, N. Mezailles, Structural transitions at the nanoscale: the example of palladium phosphides synthesized from white phosphorus, Dalton Trans., 42 (2013) 12667-12674.

[17] S. Carenco, Y. Hu, I. Florea, O. Ersen, C. Boissiere, N. Mezailles, C. Sanchez, Metal-Dependent Interplay between Crystallization and Phosphorus Diffusion during the Synthesis of Metal Phosphide Nanoparticles, Chem. Mater. 24 (2012) 4134-4145.

[18] C. Xu, Y. Liu, J. Wang, H. Geng, H. Qiu, Nanoporous PdCu alloy for formic acid electro-oxidation, J. Power Sources, 199 (2012) 124-131.

[19] A. M. Venezia, L. F. Liotta, G. Deganello, Z. Schay, L. Guczi. Characterization of Pumice-Supported Ag–Pd and Cu–Pd Bimetallic Catalysts by X-Ray Photoelectron Spectroscopy and X-Ray Diffraction. J. Catal. 182 (1999) 449-455.

[20] J. F. Moulder, W. F. Stickle, P. E. Sobol, K. D. Bomben, Handbook of X-ray photoelectron spectroscopy, Perkin-Elmer 1992.

[21] D. R. Liyanage, S. J. Danforth, Y. Liu, M. E. Bussell, S. L. Brock, Simultaneous Control of Composition, Size, and Morphology in Discrete Ni2–xCoxP Nanoparticles, Chem. Mater., 27 (2015) 4349-4357.

[22] V. Tallapally, R. J. A. Esteves, L. Nahar, I. U. Arachchige, Multivariate Synthesis of Tin Phosphide Nanoparticles: Temperature, Time, and Ligand Control of Size, Shape, and Crystal Structure, Chemistry of Materials, 28 (2016) 5406-5414.

[23] S. Cao, Y. Chen, C. C. Hou, X. J. Lv, W. F. Fu, Cobalt phosphide as a highly active non-precious metal cocatalyst for photocatalytic hydrogen production under visible light irradiation, J. Mater. Chem. A, 3 (2015) 6096-6101.

[24] Y. Zhu, S. Murali, W. Cai, X. Li, J.W. Suk, J.R. Potts, R.S. Ruoff, Graphene and graphene oxide: synthesis, properties, and applications, Adv. Mater., 22 (2010) 3906-3924.

[25] N. I. Kovtyukhova, P. J. Olliver, B. R. Martin, T. E. Mallouk, S. A. Chizhik, E. V. Buzaneva, A. D. Gorchinskiy. Layer-by-Layer assembly of Ultrathin Composite Films from Micron-Sized Graphite Oxide Sheets and Polycations. Chem. Mater. 11 (1999) 771-778.

[26] R.N. Singh, A. Singh, Anindita, Electrocatalytic activity of binary and ternary composite films of Pd, MWCNT and Ni, Part II: Methanol electrooxidation in 1M KOH, Int. J. Hydrogen Energ., 34 (2009) 2052-2057.

[27] Q. Jiang, L. Jiang, H. Hou, J. Qi, S. Wang, G. Sun. Promoting Effect of Ni in PtNi Bimetallic Electrocatalysts for the Methanol Oxidation Reaction in Alkaline Media: Experimental and Density Functional Theory Studies. J. Phys. Chem. C. 114 (2010) 19714-19722.

[28] H. Xu, B. Yan, S. Li, J. Wang, C. Wang, J. Guo, Y. Du, One-pot fabrication of N-doped graphene supported dandelion-like PtRu nanocrystals as efficient and robust electrocatalysts towards formic acid oxidation, J Colloid Interface Sci, 512 (2018) 96-104.

[29] M. Xiao, S. Li, X. Zhao, J. Zhu, M. Yin, C. Liu, W. Xing, Enhanced Catalytic Performance of Composition-Tunable PtCu Nanowire Networks for Methanol Electrooxidation, ChemCatChem, 6 (2014) 2825-2831.

[30] Y. Shen, B. Gong, K. Xiao, L. Wang, In Situ Assembly of Ultrathin PtRh Nanowires to Graphene Nanosheets as Highly Efficient Electrocatalysts for the Oxidation of Ethanol, ACS Appl. Mater. Inter., 9 (2017) 3535-3543.

[31] P. Wang, S. Yin, Y. Wen, Z. Tian, N. Wang, J. Key, S. Wang, P.K. Shen, Ternary Pt9RhFex Nanoscale Alloys as Highly Efficient Catalysts with Enhanced Activity and Excellent CO-Poisoning Tolerance for Ethanol Oxidation, ACS Appl. Mater. Inter., 9 (2017) 9584-9591.

[32] Q.Q. Xia, L.Y. Zhang, Z.L. Zhao, C.M. Li, Growing Platinum-Ruthenium-Tin ternary alloy nanoparticles on reduced graphene oxide for strong ligand effect toward enhanced ethanol oxidation reaction, J Colloid Interface Sci, 506 (2017) 135-143.

[33] K. Lee, S.W. Kang, S.U. Lee, K.H. Park, Y.W. Lee, S.W. Han, One-pot synthesis of monodisperse 5 nm Pd-Ni nanoalloys for electrocatalytic ethanol oxidation, ACS Appl. Mater. Inter., 4 (2012) 4208-4214.

[34] R. Jana, U. Subbarao, S.C. Peter, Ultrafast synthesis of flower-like ordered Pd 3 Pb nanocrystals with superior electrocatalytic activities towards oxidation of formic acid and ethanol, J. Power Sources, 301 (2016) 160-169.

[35] Z. Zhang, S. Liu, X. Tian, J. Wang, P. Xu, F. Xiao, S. Wang, Facile synthesis of N-doped porous carbon encapsulated bimetallic PdCo as a highly active and durable electrocatalyst for oxygen reduction and ethanol oxidation, J. Mater. Chem. A, 5 (2017) 10876-10884.

[36] J. Xue, G. Han, W. Ye, Y. Sang, H. Li, P. Guo, X.S. Zhao, Structural Regulation of PdCu2 Nanoparticles and Their Electrocatalytic Performance for Ethanol Oxidation, ACS Appl. Mater. Inter., 8 (2016) 34497-34505.

[37] Y. Wang, Q. He, J. Guo, J. Wang, Z. Luo, T.D. Shen, K. Ding, A. Khasanov, S. Wei, Z. Guo, Ultrafine FePd Nanoalloys Decorated Multiwalled Cabon Nanotubes toward Enhanced Ethanol Oxidation Reaction, ACS Appl. Mater. Inter., 7 (2015) 23920-23931.

[38] T. Liu, K. Wang, Q. Yuan, Z. Shen, Y. Wang, Q. Zhang, X. Wang, Monodispersed sub-5.0 nm PtCu nanoalloys as enhanced bifunctional electrocatalysts for oxygen reduction reaction and ethanol oxidation reaction, Nanoscale, 9 (2017) 2963-2968.

[39] C. W. Xu, H. Wang, P. K. Shen, S. P. Jiang, Highly Ordered Pd Nanowire Arrays as Effective Electrocatalysts for Ethanol Oxidation in Direct Alcohol Fuel Cells, Adv. Mater., 19 (2007) 4256-4259.

[40] A. L. Wang, X. J. He, X. F. Lu, H. Xu, Y. X. Tong, G. R. Li, Palladium‐Cobalt Nanotube Arrays Supported on Carbon Fiber Cloth as High‐Performance Flexible Electrocatalysts for Ethanol Oxidation, Angew. Chem. Int. Ed., 54 (2015) 3669-3673.

[41] D. Bin, B. Yang, K. Zhang, C. Wang, J. Wang, J. Zhong, Y. Feng, J. Guo, Y. Du, Design of PdAg Hollow Nanoflowers through Galvanic Replacement and Their Application for Ethanol Electrooxidation, Chem. Eur. J., 22 (2016) 16642-16647.

[42] W. Hong, J. Wang, E. Wang, Facile synthesis of PtCu nanowires with enhanced electrocatalytic activity, Nano Res., 8 (2015) 2308-2316.

[43] K. Jiang, L. Bu, P. Wang, S. Guo, X. Huang, Trimetallic PtSnRh Wavy Nanowires as Efficient Nanoelectrocatalysts for Alcohol Electrooxidation, ACS Appl. Mater. Inter., 7 (2015) 15061-15067.

[44] H. Mao, L. Wang, P. Zhu, Q. Xu, Q. Li, Carbon-supported PdSn–SnO2 catalyst for ethanol electro-oxidation in alkaline media, Int. J. Hydrogen Energy, 39 (2014) 17583-17588.

[45] W. Du, K.E. Mackenzie, D.F. Milano, N.A. Deskins, D. Su, X. Teng, Palladium–Tin Alloyed Catalysts for the Ethanol Oxidation Reaction in an Alkaline Medium, ACS Catal., 2 (2012) 287-297.